Digital Twin Model Development for Mitigating Floating Offshore Wind Turbine Motions Due to Wave Actions

Yuksel R. Alkarem[1]*,Kimberly Huguenard* [1]*,Richard W. Kimball*[2]*,Babak Hejrati*[2]*,Andrew Goupee* [2]*,*
Shawn Albertson[3]*,Jacob Fontaine*[3]*,Stéphan T. Grilli*[3]*,Stephanie Steele*[3] *and Jason Dahl*[3]
(1) Department of Civil and Environmental Engineering, University of Maine, Orono, ME, USA
(2) Department of Mechanical Engineering, University of Maine, Orono, ME, USA
(3) Department of Ocean Engineering, University of Rhode Island, Narragansett, RI, USA

ABSTRACT

The coupled action of wind and wave on the stability of floating offshore wind turbines (FOWT) tremendously affects the lifespan of these energy systems and their energy output. Passive control systems reduce such loads but can only mitigate the loading over a small range of excitation frequencies. To improve this, an active control system (ACS) is needed. The aim of this research is a digital twin proof of concept allowing the diagnosis of current and upcoming environmental events and re-tuning the ACS based on a mass-spring damper system (TMD) to minimize wave-induced response at the frequency range of interest. This is accomplished through a series of numerical investigations supported by laboratory measurements in a wave basin made on a scale model of a 15MW FOWT. The numerical models are implemented via the multi-physics, multi-fidelity code: OpenFAST, that enables coupled nonlinear aero-hydro-servo-elastic simulation in time domain. The code is modified to enable ACS implementation and ease of communication between the controller and OpenFAST. After validating the model, an open-loop controller is designed to allow multiple stiffness and damping entries targeting first-order wave-frequency region. Two methods of data acquisition are investigated: the Current Sea-State Controller (CSSC) where sea-state prediction is governed by past wave elevation data points using a polynomial weighted buffer that leverages more recent data, and the Future Sea-State Controller (FSSC) that, additionally utilizes reconstruction/prediction model of the upcoming wave to investigate the effect of reduced latency in the controller response. Both controllers are optimized through a genetic algorithm scheme. Preliminary results show an advantage for the latter controller in reducing wave excitations ranging between 10s to 20s under varying sea-state. While the magnitude of reduction is defined by the specific arrangement of the TMD system studied, this study builds the foundation of a more sophisticated digital twin system with concepts such as control co-design in its core.

KEYWORDS: Hydrodynamics modeling; dynamic positioning; control; model predictive control; model test.

INTRODUCTION

Wind energy is being recognized as a central factor in attaining Paris agreement (COP21) goals of 1.5 C global warming by the year 2100. Specifically, offshore wind energy is the most commercially well-established marine renewable form with a relatively mature technology (Astariz and Iglesias, 2016). This motivates more industry to be included in the picture and is the reason behind a year-over-year (YoY) growth of 12% in the year 2021 which was the wind industry's second-best year after 2020. Onshore wind market added 72.5 GW worldwide whereas offshore installations represented 22.5% of all new installations in the year 2021, bringing the world's total offshore capacity to 57GW (Council, 2022).

As offshore wind is transitioning towards floating technologies, the platform rigid-body motion becomes an urgent issue in the design and analysis stage (Alkarem, 2020). Hence, numerical and experimental applications are necessary to understand this multi-faceted problem (Martin et al., 2014; Viselli et al., 2015). For instance, the sea-to-land ratio of fore-aft tower base bending moment fatigue loads is 2.5 for spar-type and 7.0 for barge-type platform (Jonkman, 2009). Therefore, innovation that leads to response reduction is critical in the design of floating offshore wind turbines (FOWT) and active control system becomes a necessity. While active control systems have been extensively researched for the turbine control (Raach et al., 2014), strategies for minimizing wave-induced rigid body motion of the platform are usually based on passive techniques such as tuned mass dampers (TMDs) that can be optimized to mitigate vibrations/motions of certain frequencies (Villoslada et al., 2020; Stewart and Lackner, 2014). These dampers can be either situated in the nacelle (Ding et al., 2019; Lackner and Rotea, 2011b), in the platform (Kimball et al., 2022), or both (Yang and He, 2020) and can be either passive (Lackner and Rotea, 2011a) or active (Namik et al., 2013). In general, active retuning of TMDs show better reduction in motion at the expense of active power and mass stroke distance which can be unrealistic for practical applications.

As digital technology related solutions are invading every industry, research in its early stages is taking place worldwide to enhance the efficiency and productivity of offshore operations such as in oil and gas (OG) industry (LaGrange, 2019) and in fault diagnosis and operation optimiza-

tion of offshore wind turbines (Mehlan et al., 2022). In this research, digital twin is a loose term that translates to the active feed of the short-term predicted wave elevation to the controller, how the platform would respond to that input, and the active retuning of the TMD to minimize that motion. Ma et al. (2018) has demonstrated the important role the control algorithm has on reducing the platform's response and developed a forecasting algorithm for the wave elevation and wave excitation loads. Desmars et al. (2020) investigated the accuracy of a phase-resolved, predictive model based on data obtained from an array of wave gauges that represent a typical spatial sampling of an optical sensor (e.g., LIDAR). Active control systems on a floating system can be applied over different time scales. Short-term scaling on the order of individual wave variation such as the work done by Steele et al. (2023), or over long-term scales on the order of local wave spectral variation such as the work presented in this paper.

SEA-STATE (SS) VARYING TEST DESIGN

The basic SS building blocks are described in Table 1. The wave surface elevations are irregular waves described by the Joint North Sea Wave Project (JONSWAP) spectrum that describes a SS through three parameters, the significant wave height, H_s, the peak wave period, T_p, and the peak enhancement factor, γ.

test ID	SS1	SS2	SS3	SS4
H_s (m)	3.1	6.3	8.1	10.9
T_p (s)	8.96	11.46	12.8	14.2
γ	1.8	2.75	2.75	2.75
F_{low} (Hz)	0.0599	0.0514	0.0455	0.0411
F_{high}(Hz)	0.3540	0.2752	0.2531	0.2557
C_{cal}	1.1856	1.0580	1.0397	1.0209

Table 1: SS building block (JONSWAP spectra)

Wave Frequency Spectrum Generation

For each of the wave spectrum described above, waves at frequencies with energy less than 0.1% of the peak are cut off. A coefficient for calibrating the wave amplitude is also calculated through comparing the generated significant wave height from previous experiments at the W2 basin with the designated values, The low cut-off frequency, F_{low}, the high cut-off frequency F_{high}, and the calibration coefficient for wave height, C_{cal} are also shown in Table 1. The unscaled JONSWAP spectrum is computed as follows:

$$
\begin{aligned}
S(f) &= \frac{\alpha g^2}{\omega^5}\exp\left[-\frac{5}{4}\left(\frac{\omega_p}{\omega}\right)^4\right]\gamma^r,\\
r &= \exp\left[-\frac{(\omega-\omega_p)^2}{2\sigma^2\omega_p^2}\right],\\
\sigma &= \begin{cases} 0.07 & \omega <= \omega_p \\ 0.09 & \omega > \omega_p. \end{cases}
\end{aligned}
\tag{1}
$$

where $\omega_p = 2\pi/T_p$, and ω is a random selection of frequencies in rad/s between the lower and higher limits with a discretization value of $d = 500$. α is kept constant of 320.

Reduced Testing Duration

The recommended minimum value by DNV (reference) for an irregular wave test is 1hr full scale. As a verification, the error between the zero

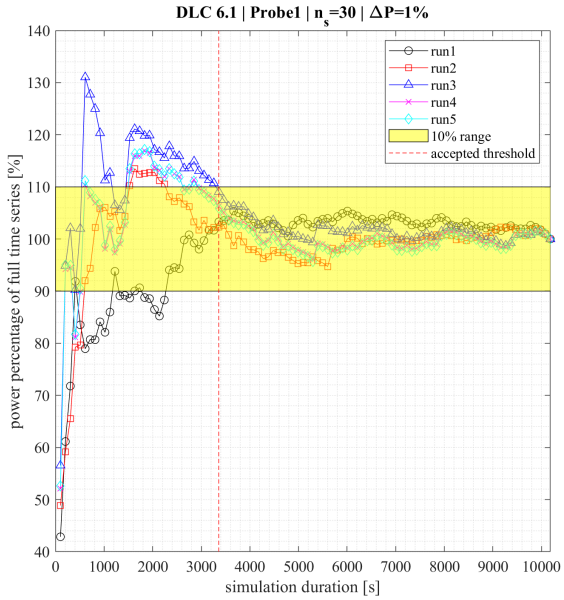

Fig. 1: relative wave spectra as a function of the duration run of 5 different seed runs in the basin.

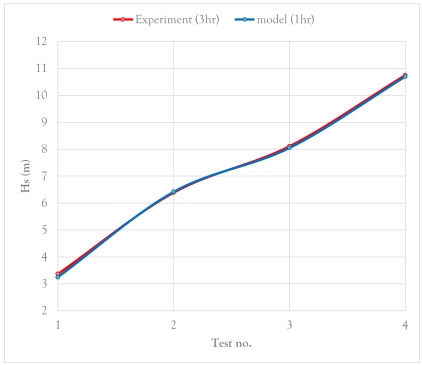

Fig. 2: significant wave height for 3hr and 1hr running time of all SS building block tests.

moment of the wave spectrum, m_0, of a portion of the SS spectrum and a full (3hr) spectrum is computed:

$$
\begin{aligned}
e(t) &= \frac{\left(m_0^t - m_0^{3hr}\right)}{m_0^{3hr}},\\
m_0^t &= \int_{f=f_{low}}^{f=f_{high}} S^t(f)df,\\
m_0^{3hr} &= \int_{f=f_{low}}^{f=f_{high}} S^{3hr}(f)df
\end{aligned}
\tag{2}
$$

where $S^t(f)$ is the JONSWAP spectrum of wave data from $t = 0$ to t. This analysis is run over various generated wave surface elevation in the basin of different seeds. As shown in Figure1, after an hour of running, the relative error drops down to the 10% range. Numerically, The averaged values of H_s and T_p for the four tests are shown in Figures 2 and 3 for 1hr and 3hr running time. Therefore a 1hr spectrum is considered representative of the SS.

SS-Varying Test Description

The test simulates a gradual increase of the SS extremity (from SS1 to SS4) with a ramped duration between the blocks of $h = 30$s full scale.

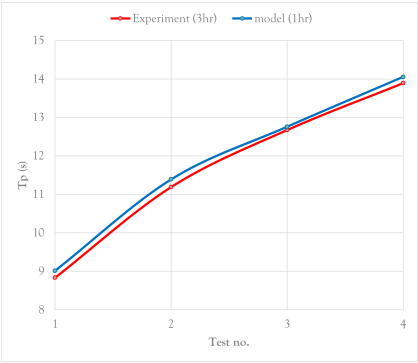

Fig. 3: wave peak period for 3hr and 1hr running time of all SS building block tests.

The choice of this ramping value is selected to cover one cycle of the degree of freedom (DOF) of interest, pitch. Albeit, it might be worthy to investigate the effect of the ramped value on the behavior of the system and the ability of the Digital Twin to detect the variation in the wave environment. The transitioning of the SS is dealt with using linear shape functions of $N_1 = \frac{t_i - t}{h} + 1$ for the dying SS and $N_2 = \frac{t - t_i}{h}$ for the newly born SS where t_i is the beginning of ramping and t is the variation of time during ramping. The final results are super-positioned. The wave height and wave period in the test are shown in Figure 4.

SS DETECTION SCHEME AND OPTIMIZATION

The SS parameters shown in Figure 4 are the desired values, and minimizing the difference between the desired SS and the predicted SS is the objective function. Three different schemes are designed: Past, PSSC, Current, CSSC, and Future FSSC detectors listed from the simplest to more complex. Figure 5 illustrates the logic of these detectors in which the shaded area is the wave data being analysed for the predictor and the solid curves/lines represent the weight function in time. The red data points are in future. It is assumed that the predicted waves in future matches perfectly the designed wave train.

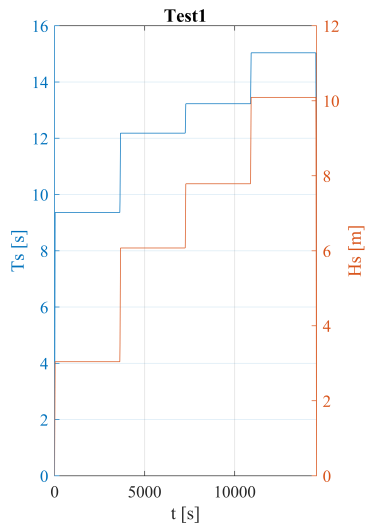

Fig. 4: significant wave height and wave peak period of the designed SS-varying tests.

Parameter Description

The first parameter, $P1 = \Delta t_P$ describes the data acquisition time in the past to be used in the zero-up crossing method to determine the significant wave period, T_s, which is defined as the average of the third biggest wave period in the time series. The second parameter, $P2 = b\Delta t_P/2$ controls the weight function, $w_P(t)$ that is multiplied by T_s. A constant value of $w_P = 1$ describes the first detection scheme, PSS. Meanwhile CSS uses a polynomial function that gives more weight to more recent data:

$$w_P(t) = at^2 + bt + c, \tag{3}$$

subject to temporal boundary conditions:

$$\begin{aligned} w_P(t - \Delta t_P) &= 0, \\ w_P(t) &= 1, \\ \left.\frac{dw}{dt}\right|_t &= 2a(t) + b > 0, \\ \left.\frac{dw}{dt}\right|_{t-\Delta t_P} &= b > 0 \end{aligned} \tag{4}$$

Applying these conditions we get

$$\begin{aligned} a &= \frac{1 - b\Delta t_P}{\Delta t_P^2}, \\ 0 < b &< \frac{2}{\Delta t_P}, \\ c &= 0 \end{aligned} \tag{5}$$

Therefore, ranging $P2$ between 0 and 1 controls the shape of the polynomial function:

$$b = P2 \times \frac{2}{\Delta t_p}. \tag{6}$$

When $P2 = 1/2$, the weight function is linear.

As for the FSS detector, two additional parameters are added that governs the upcoming wave data. Just like $P1$, $P3 = \Delta t_F$ depicts the duration in future data points to be included in predicting T_p, and $P4 = w_F$ is a weight constant that leverages the forecast data by having $w_F > 1$.

It is desirable to optimize the values of these parameters. To this effect, we apply a genetic algorithm (GA) to find the optimal values of these parameters that would minimize the cost function which is the average of the two-norm of the difference between the designed SS parameters, namely H_s and T_p, and the estimated values:

$$C = \frac{1}{N}\left(\frac{1}{2}\left(||H_s^{predicted} - H_s^{target}|| + ||T_p^{predicted} - T_p^{target}||\right)\right) \tag{7}$$

where N is the number of comparison points throughout the test. The upper and lower limits for the parameters are shown in Table 2. The upper limit for $P1$ is selected to be a full hour as this is the duration of SS segments in the tests. Since the definition of the forecast method is loose in this study, $P3$ constraints cannot be pin-pointed. However, by definition, the range of $P3$ is much smaller than past data acquisition (predicting a small portion of the wave coming ahead), so an arbitrary choice of approximately $10 \times T_p \approx 120$s is selected and a lower limit of 30s. Since $P4$ is the leveraging parameter of future data (gives more wright to future data), it must be greater than 1. However, it is not clear what would the upper limit be. Basic sensitivity analysis (not shown here for conciseness) has shown that extremely high values of $P4$ can harm the predictor (i.e. increase the objective function) by introducing a lot of noise. As for the general setup of the GA, maximum generation is set at 40 for CSS and 60 for FSS since it has more parameters (i.e. more number of genes). The number of population is kept the same at 60, and the number of genes are

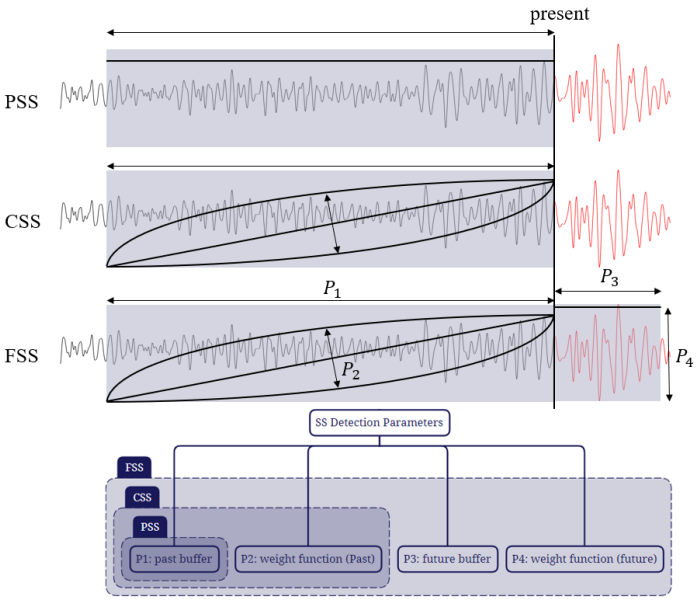

Fig. 5: A schematic for SS detection schemes and their parameters.

limit	$P1$	$P2$	$P3$	$P4$
lower	100	0	30	1
upper	3600	1	120	5

Table 2: lower and upper limit of the SS detection parameters

2 and 4 for CSS and FSS, respectively. The outcome is described in the results in Table 3. The optimization scheme is run for two types of tests, a gradual extremity variation and it is the one we are focusing here, and another test of calm condition followed by a sudden storm surge. $P1$ for the first test is quite different than the second test. When the SS increases gradually in extremity, the data acquisition is long, but with sudden SS change as in test 2, the optimum data acquisition time is shrunk. Additionally, the shape of the weighting function takes a concave curvex‘ for test 1 and a convex curve for test 2. The polarity of these results is interesting. Figure 6 illustrates the resulting estimated wave period, T_e for all detection schemes for test 1.

DAMPING COEFFICIENT LOOKUP TABLE INTERPOLATION

Simplified Time-Domain OpenFAST model

The search for an optimum damping ratio given a stiffness value for the TMDs can be quite extensive. To allow the GA to run multiple cases and select the best fit, a simplified OpenFAST model is built and being called at every iteration by the algorithm. It is simplified by increasing time-step, decreasing output tabulation, and de-activating the DoFs that are

Detection scheme—test	$P1$	$P2$	$P3$	$P4$	Obj
CSSC—1	3533.40	0.00	N/A	N/A	2.05
CSSC—2	659.74	0.87	N/A	N/A	2.37
FSSC—1	3543.23	0.00	113.59	5.00	1.96
FSSC—2	663.97	0.99	80.96	4.97	2.36

Table 3: lower and upper limit of the SS detection parameters

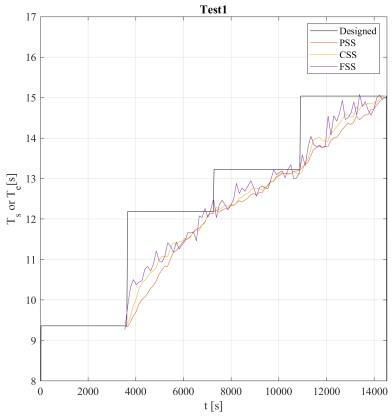

Fig. 6: estimated wave period in contrast with the designed wave period.

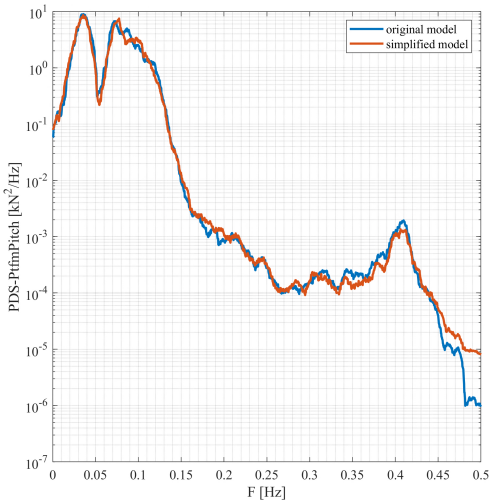

Fig. 7: original model v. simplified version PSD of the tower base fore-aft bending moment response in 1hr, 50-year return period wave case simulation.

not of interest, such as sway, heave, roll, and yaw. The DoF that is used to check the validitiy of this model is the tower-base fore-aft bending moment which is mainly driven by the pitch response. This simplified model is only used to obtain the lookup table and not in the actual validation. A 1hr frequency-domain comparison between the original model and the simplified version is shown in Figure 7. While the simplified model is 40% faster, the standard deviation in pitch response only changed by 2.3%.

Wave Region Selection for Optimization

Running the simulation for a full hour is time consuming, instead, only a portion of the wave train is selected. The region is selected so that it covers the maximum wave height in the wave elevation history, H_{max}. Then, to present a fair comparison for different test blocks, the number of waves in the selected region to be scrutinized, x_w is kept the same (not necessarily the same duration). Additionally, a ramping initiation is introduced. Therefore, the selected region is defined as the temporal range $H_{max} - x_w/2 - T_{ramp} < t < H_{max} + x_w/2$. Figure 8 demonstrate the selection of the wave region the GA operates over.

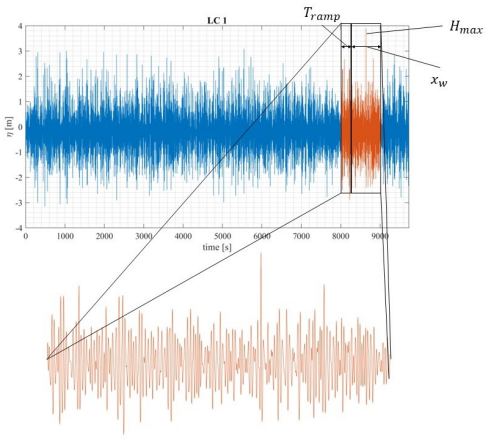

Fig. 8: wave region selection for obtaining C lookup table.

GA Optimization for Damping Ratio

The stiffness value, K is governed by the estimated wave period, T_e, by the SS detection scheme described in the previous section:

$$K = \omega_e^2 m$$
$$\omega_e = \frac{2\pi}{T_e} \tag{8}$$

where $m = 686000$kg is the mass of the TMD for the studied configuration. To determine the corresponding damping value, one can use the following relation

$$C = 2\zeta\sqrt{Km} \tag{9}$$

where ζ is the damping ratio and is the target of this optimization scheme. The objective (fitness function) is the pitch response of the system. The constraints for the damping value are 0 and 1 to keep the system underdamped. The resulting optimization based on the test blocks are described in Table 4.

test ID	SS1	SS2	SS3	SS4
ζ	0.023	0.064	0.876	0.557

Table 4: Optimum ζ for various test blocks

The K & C data are then interpolated for estimated SS that lie in-between. An example of the TMD parameter variation for test 1 is shown in Figure 9.

EXPERIMENTATION

Wave Calibration

The 16 wave pedals in the W2 wave basin situated at the Advanced Structures and Composites Center at UMaine is calibrated to match the power spectrum density of the theoretical wave surface elevation to the spectrum of the wave probe data in the basin. For the sake of conciseness, the calibrated PSD for one of the seeds is delineated in Figure 10. The two spectra agree well with some slight discrepancies presented in higher frequencies.

TMD Set-Point Characterization

To create a characteristic curve for the natural frequency and damping ratio as a function of the applied spring stiffness for each of the three TMDs

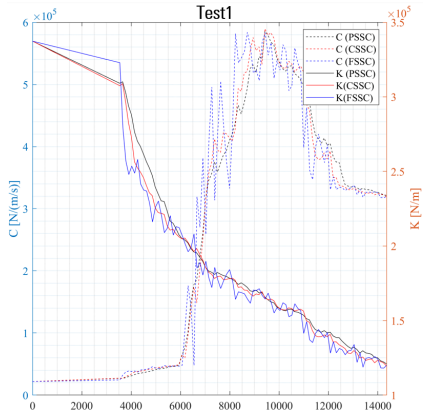

Fig. 9: K & C variation for test 1 based on the SS estimator for K and lookup table for C.

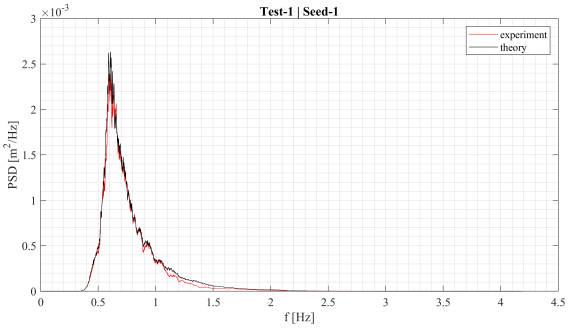

Fig. 10: comparison of the power spectrum density of the wave elevation data between wave probe data and theory

situated in the hull, a sweep of varying spring and damping values is conducted using a System Identification (SID) methodology to extract the dynamic system properties of the physical system. This method applies a synthetic force based on pink noise excitation. Fast Fourier transform (FFT) is then applied to the setpoint force and position time series. The resulting response is compared to the theoretical transfer function and calibration is applied as following:

$$f_0 = a \times k^b \tag{10}$$

where f_0 is the targeted (theoretical) frequency, k is the actual TMD stiffness value to be calibrated, and a and b are the calibrating parameters. The characterization test resulting in a and b values shown in Table 5 and the test setup is shown in Figure 11.

TMD #	1	2	3
a	0.1687	0.1938	0.1789
b	0.4011	0.3714	0.3957

Table 5: summary of the calibrating parameters resulting from TMD characterization tests

Characterization Tests

These tests ensure the system is setup right and checks the static equilibrium, mooring stiffness, and the natural frequency of the system.

The static position of the system is checked every time the floater is removed and placed in the basin. The average static position is reported in Table 6. The mooring stiffness is tested by slowly forcing static offset

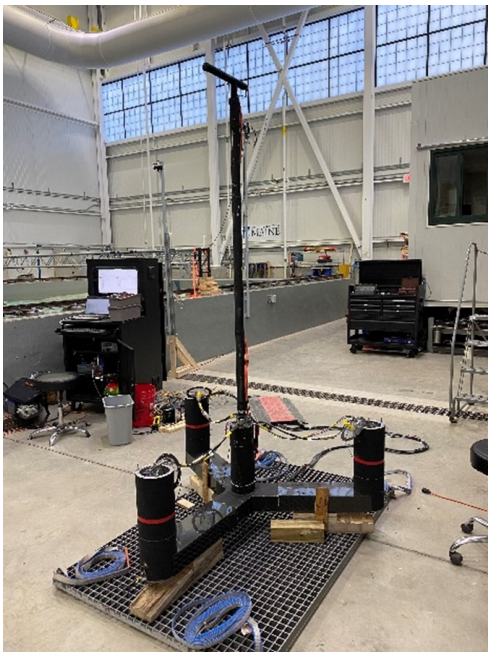

Fig. 11: TMD characterization test setup

in the X direction (both positive and negative) and measuring tensions in the three cables. The positive offset is shown in Figure 12. The values at excursion 0 are the pretension values. There can be seen a slight differences in these values but in lab scale, it becomes nearly impossible to distinguish the difference. In this offset test, the structure is being drifted further away from the bow anchor, hence the higher tension in the bow cable and lower tensions in the stern cables.

DOF	X	Y	Z	RX	RY	RZ
value	0.00	0.00	-0.29	-0.69	1.34	-1.17

Table 6: average static position of the system

The free decay tests are performed on the two degrees of freedom of interest; heave and pitch. Four repetitions are performed. The damping ratio as a function of initial cycle amplitude is extracted and can be used in the future to compare/calibrate numerical models. The response of one repetition is plotted in Figure 13. These oscillations have expected periods of 20.67s and 27.95s for heave and pitch, respectively.

Irregular Wave Sea-State Varying Tests

The platform is then excited by stochastic wave input of gradually increasing extremity (test 1). A script is written to divide the resulting response based on the extremity of the loading, the superposition of which must give the total response as illustrated in Figure 14 for the fixed case (TMDs' sole influence to the dynamics of the system is their mass). This gives insight as how different control methods affect responses at various extreme conditions.

For the sake of comparison, the response spectra (the output) are normalized by the wave elevation surface spectrum (the input) to extract the response amplitude operator (RAO). However, RAO can give erroneous results if the input does not have enough energy (frequencies outside the wave region). Therefore, to ensure the RAO is only applied at the wave region, a filter is applied to erase output data corresponding to wave spectra that is below or equal to 5% of the spectral peak. This results in RAO

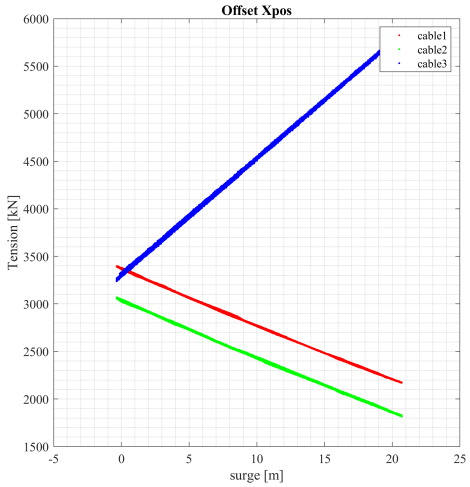

Fig. 12: measured tension values in all three cables as a function of horizontal excursion in the X direction (positive)

data such as the one shown in Figure 15 where SS#4 has wave energy up to 20sec (therefore responses can be compared up to 20sec) while wave energy at SS#1 dies at around 13sec. The RAO is then divided into frequency bins and the bin area under the spectral curve, dA is used as comparison parameter.

CSSC/FSSC v. fix Figure 16 illustrates the ratio of the bin area of the different control schemes (either CSSC or FSSC) to the bin area of the fixed case, dA_1/dA_2. If the ratio is below unity, reduction in the response is in favor the control method and vice versa. The response at various SS is distinguished by colors and only plotted at the proper frequency region for each sea-state. Both CSSC and FSSC controller exacerbate the responses at low wave periods. At higher periods, the response is enhanced with FSSC performing better than CSSC. interestingly, heave and pitch for the most extreme SS with CSSC enabled is even worse than the fixed condition.

CSSC v. FSSC Figure 18 demonstrates a different perspective to the same results with the fixed controller out of the picture and only comparing CSSC with FSSC. Blue regions are enhancements in favor of FSSC and red is in favor of CSSC. Here, the pattern can be easily observed. CSSC performs better at lower periods while FSSC performs better at higher ones. However, it is not wise to consider low period and high pe-

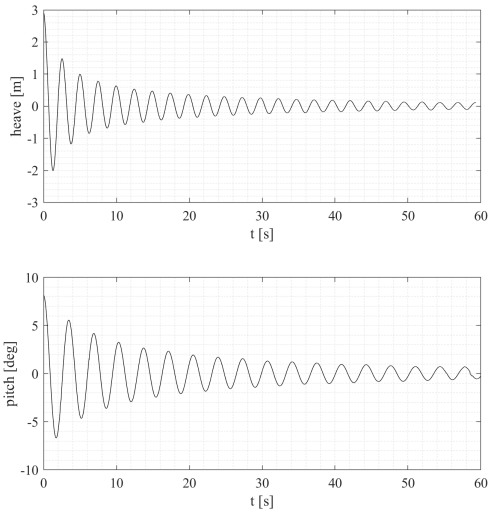

Fig. 13: free decay test in heave and pitch degree of freedom

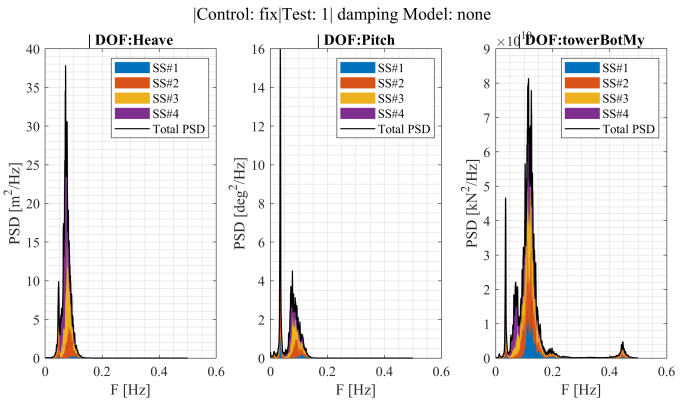

Fig. 14: SS-based divided responses of the fixed case

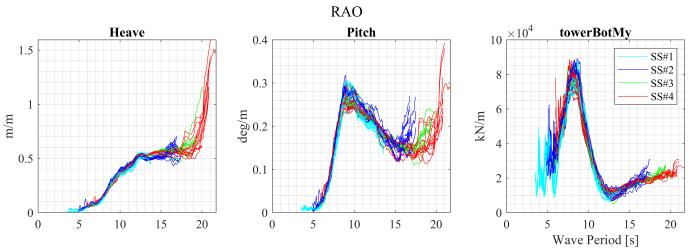

Fig. 15: RAO at or higher than 5% input threshold

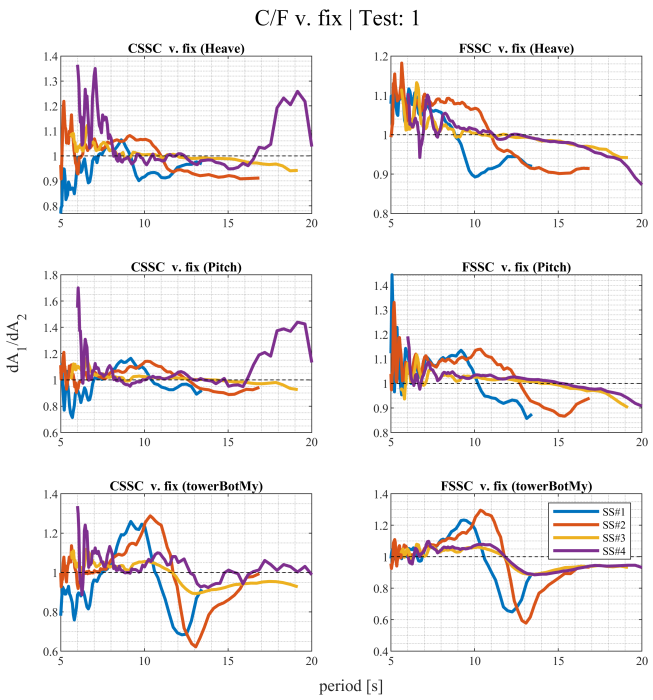

Fig. 16: response of CSSC and FSSC v. fix

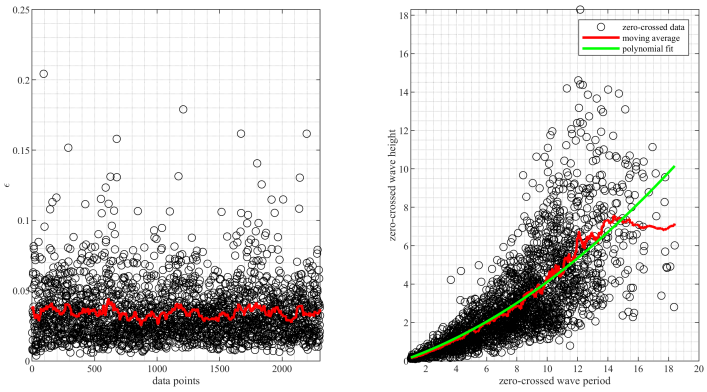

Fig. 17: wave steepness of the zero-crossed wave elevation data (left) and polynomial relationship between individual wave period v. wave height for one test

riod excitations equal since higher periods hold more energy to them and reducing the energy there is more critical than lower periods. From linear wave theory, we know that through the deepwater dispersion relation;

$$L \propto T^2 \tag{11}$$

and given a constant wave steepness, ε,

$$H \propto T^2. \tag{12}$$

Since

$$E = \frac{1}{8}\rho g H^2, \tag{13}$$

that makes

$$E \propto T^4. \tag{14}$$

The above assumption that the wave steepness is constant is investigated by applying zero-crossing to the wave elevation data and measuring the moving average over the data. This is illustrated for one of the tests in the left subplot of Figure 17. The moving average suggests that despite variations in the extremity of the wave, the overall wave steepness remains more or less constant. The correlation between the individual wave heights and wave periods after applying zero-crossing is also shown in the right subplot of the same figure with the 2^{nd}-order polynomial fit and a moving average. The moving average oscillates around the fit. Discrepancies start to occur at very high wave period/height due to the scarcity of the data. The general trend is in fact of 2^{nd}-order polynomial nature.

This allows us to penalize/reward exacerbation/improvement in the response, accordingly. The resulting weighted average as a function of SS and of DOF of interest is given in Table 7. The weighted average is mostly below 1 favoring FSSC and the average value is 0.978. This may not seem to be revolutionary in response reduction but is a proof of concept that having the knowledge of the upcoming wave and preparing for it can actually make a positive difference.

	SS#1	SS#2	SS#3	SS#4	Average
Heave	1.009	1.003	0.998	0.918	0.982
Pitch	1.007	1.001	0.994	0.881	0.971
TwrBsMyt	1.002	0.986	0.995	0.940	0.981
Average	1.006	0.997	0.996	0.913	0.978

Table 7: weighted average of dA_1/dA_2

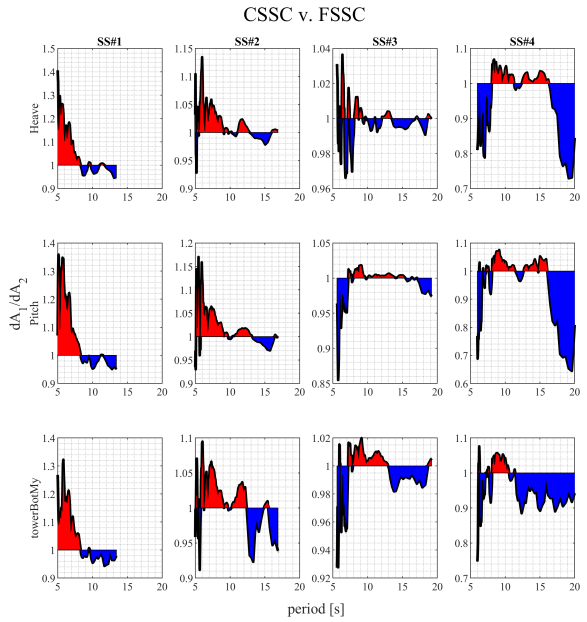

Fig. 18: response of CSSC v. FSSC

CONCLUSION

A crucial part of the digital twin development is to ensure the system is up-to-date with its surroundings and to adapt accordingly. This research shows that actively re-tuning the mass dampers at the hull can impact the response. If the re-tuning process takes into consideration the spatio-temporally forecasted wave at the hull, the resulting response undergoes an improvement in the lower wave frequency region where wave energy is higher (stormy waves) when compared to the fixed TMD scenario or the current SS controller in which the controller only knows the past and the current state of the sea at the hull. This research is the foundation to build more sophisticated algorithms that serves as a design tool (optimization and control-co design (CCD)) that aims to lower the levelized cost of energy (LCOE) by maximizing power output and minimizing fatigue on the whole wind farm and its individual components, and later as a real-time observer/controller of the physical system.

REFERENCES

Alkarem, Y. (2020). *Numerical examination of floating offshore wind turbine and development of an innovative floating platform design*. PhD thesis, Izmir Institute of Technology (Turkey).

Astariz, S. and Iglesias, G. (2016). Co-located wind and wave energy farms: Uniformly distributed arrays. *Energy*, 113:497–508.

Council, G. W. E. (2022). Floating offshore wind—a global opportunity. *The Global Wind Energy Council*.

Desmars, N., Bonnefoy, F., Grilli, S., Ducrozet, G., Perignon, Y., Guérin, C.-A., and Ferrant, P. (2020). Experimental and numerical assessment of deterministic nonlinear ocean waves prediction algorithms using non-uniformly sampled wave gauges. *Ocean Engineering*, 212:107659.

Ding, Q.-w., Li, C., Cheng, S.-s., Hao, W.-x., Huang, Z.-q., and Yu, W. (2019). Study on tmd control on stability improvement of barge-supported floating offshore wind turbine based on the multi-island genetic algorithm. *China Ocean Engineering*, 33(3):309–321.

Jonkman, J. M. (2009). Dynamics of offshore floating wind turbines—model development and verification. *Wind Energy: An International Journal for Progress and Applications in Wind Power Conversion Technology*, 12(5):459–492.

Kimball, R., Robertson, A., Fowler, M., Mendoza, N., Wright, A., Goupee, A., Lenfest, E., and Parker, A. (2022). Results from the focal experiment campaign 1: turbine control co-design. In *Journal of Physics: Conference Series*, volume 2265, page 022082. IOP Publishing.

Lackner, M. A. and Rotea, M. A. (2011a). Passive structural control of offshore wind turbines. *Wind energy*, 14(3):373–388.

Lackner, M. A. and Rotea, M. A. (2011b). Structural control of floating wind turbines. *Mechatronics*, 21(4):704–719.

LaGrange, E. (2019). Developing a digital twin: The roadmap for oil and gas optimization. In *SPE Offshore Europe Conference and Exhibition*. OnePetro.

Ma, Y., Sclavounos, P. D., Cross-Whiter, J., and Arora, D. (2018). Wave forecast and its application to the optimal control of offshore floating wind turbine for load mitigation. *Renewable Energy*, 128:163–176.

Martin, H. R., Kimball, R. W., Viselli, A. M., and Goupee, A. J. (2014). Methodology for wind/wave basin testing of floating offshore wind turbines. *Journal of Offshore Mechanics and Arctic Engineering*, 136(2).

Mehlan, F. C., Nejad, A. R., and Gao, Z. (2022). Digital twin based virtual sensor for online fatigue damage monitoring in offshore wind turbine drivetrains. *Journal of Offshore Mechanics and Arctic Engineering*, 144(6):060901.

Namik, H., Rotea, M., and Lackner, M. (2013). Active structural control with actuator dynamics on a floating wind turbine. In *51st AIAA Aerospace Sciences Meeting Including the New Horizons Forum and Aerospace Exposition*, page 455.

Raach, S., Schlipf, D., Sandner, F., Matha, D., and Cheng, P. W. (2014). Nonlinear model predictive control of floating wind turbines with individual pitch control. In *2014 American Control Conference*, pages 4434–4439. IEEE.

Steele, S., Albertson, S., Fontaine, J., Dahl, J., Grilli, S., Hashemi, R., Alkarem, Y., Kimball, R., and Hejrati, B. (2023). Active control of the wave-induced motions of a float: Real-time simulations with a digital twin and experimental validation. *In Proc. 33rd Intl. Offsh. and Polar Engng. Conf. ISOPE*.

Stewart, G. M. and Lackner, M. A. (2014). The impact of passive tuned mass dampers and wind–wave misalignment on offshore wind turbine loads. *Engineering structures*, 73:54–61.

Villoslada, D., Santos, M., and Tomás-Rodríguez, M. (2020). Inerter-based passive structural control for barge floating offshore wind turbines. *IFAC-PapersOnLine*, 53(2):12358–12363.

Viselli, A. M., Goupee, A. J., and Dagher, H. J. (2015). Model test of a 1: 8-scale floating wind turbine offshore in the gulf of maine. *Journal of Offshore Mechanics and Arctic Engineering*, 137(4).

Yang, J. and He, E. (2020). Coupled modeling and structural vibration control for floating offshore wind turbine. *Renewable Energy*, 157:678–694.